ASIAN JOURNAL OF CIVIL ENGINEERING (BHRC) VOL. 16, NO. 5 (2015)
PAGES 681-708

AN EFFICIENT THERMO–MECHANICAL CONTACT ALGORITHM FOR MODELING CONTACT–IMPACT PROBLEMS

A.R. Khoei*, H. Saffar and M. Eghbalian
Center of Excellence in Structures and Earthquake Engineering, Department of Civil Engineering, Sharif University of Technology, P.O. Box. 11365-9313, Tehran, Iran

Received: 10 February 2015; **Accepted:** 15 April 2015

ABSTRACT

In this paper, the thermo-dynamic analysis of contact–impact problem is presented in the large deformation of hyperelastic material based on the Taylor-Galerkin method. The technique is applied for the time domain discretization of thermo-dynamic governing equations in the advection-diffusion problems. The impenetrability condition and frictional contact constraints are fulfilled by imposing the augmented-Lagrange technique for non-matching contact surfaces. The Taylor-Galerkin method is employed to describe the advection-diffusion effect in the numerical solution of parabolic equation of unsteady heat transfer condition. The effect of temperature is taken into account in the stress field by satisfying the free energy function. The normal and tangential forces at the contact surface are related to the temperature and heat conductivity. Numerical examples are presented to demonstrate the accuracy and efficiency of the proposed computational algorithm in large deformation thermo-dynamic analysis of contact–impact problems.

Keywords: Contact–impact; thermo-dynamic model; augmented-Lagrange method; Taylor-Galerkin technique; large deformation.

1. INTRODUCTION

In many industrial applications, numerical modeling of a system subjected to the thermo-dynamic loading with frictional contact surfaces and heat flux generation, in the framework of computational structural mechanics is still considered as a challenging task, particularly in high speed processes. The prediction of temperature and stress fields in various manufacturing processes, such as the hot metal forming, hot powder compaction, heat exchanger and metal drilling is of considerable importance because ignoring the reciprocal effects of temperature and stress fields lead to impractical simulation of natural problems.

*E-mail address of the corresponding author: arkhoei@sharif.edu (A.R. Khoei)

The thermo-mechanical behavior of contact problem must be properly modeled in the contact of two bodies. The contact may happen due to mechanical loading or thermal loading produced by the non-homogeneous thermal expansion, or contraction. In the thermo-mechanical contact friction problem, constraints are generally categorized into two groups. The first group is concerned with the kinematic constraints of deformation expressed as the impenetrability constraints and the frictional behavior of bodies at the contact zone as the stick/slip behavior. The second group consists of thermal constraints at the contact surfaces, in which the thermal contact resistance (TCR), the partition coefficient and the frictional heating due to energy dissipation are considered as thermal parameters. The practical treatment of this problem is originally proposed by Barber [1] and Cooper et al. [3] by considering the constitutive thermal behavior of contact problems.

The finite element treatment of contact problem is commonly concerned with non-matching meshes, which is due to non-conforming discretization, or large relative displacement of contact bodies. The implementation of contact constraints between two bodies can be performed using the standard penalty method [22], or the classical Lagrange multiplier technique [2]. The physical deficiency of the penalty method in satisfying the impenetrability conditions and some practical disadvantages of the Lagrange multiplier method lead to the combination of these two approaches. As a result, the perturbed Lagrange and the augmented Lagrange techniques were proposed and applied in the finite element method [26]. The significance of the finite element treatment of multibody, large deformation frictional contact problems regarding large scale computations was outlined by Laursen and Simo [16]. A rate-dependent constitutive model for the kinetic sliding of frictional interfaces was proposed by Laursen and Oancea [15] in the context of a convected reference frame for large deformation contact problems. A methodology for the solution of unilateral contact problem with non-associated threshold friction in large deformation frictional contact was performed by Pietrzak and Curnier [23] for treating the contact and friction inequality constraints. A numerical strategy for contact smoothing algorithm in large deformation was presented by Padmanabhan and Laursen [20] to solve the nonphysical oscillations in contact forces and difficulties associated with the discontinuities in the contact surface geometry. The analysis of large deformation contact problems with the Coulomb friction law between two hyperelastic bodies was performed by Feng et al. [7] by means of the augmented Lagrangian method. A mortar contact formulation was proposed by Yang et al. [28] in the solution of large deformation–large sliding frictional contact problems for treating the non-smoothness in the contact geometry. A finite element model based on oriented volumes was developed by Halikal and Hjelmstad [8] for non-smooth contact problems that guarantee the conservation of the total energy during impact using the Lagrange multiplier method. A frictional contact formulation for large deformation problems was presented by Oliver et al. [19], where the contact constraints were formulated using the contact domain method as a fictive intermediate region connecting the potential contact surfaces of deformable bodies. An enriched finite element method based on the X-FEM technique was developed by Khoei and Mousavi [14] for large deformation–large sliding contact problems. The application of NURBS-based isogeometric analysis was recently performed by de Lorenzis et al. [4] to the Coulomb frictional contact problems in the context of large deformations using the mortar-based approach.

In thermo-mechanical analysis of contact friction problem, a proper contact formulation

must be utilized to ensure the accuracy of the computed pressure and thermal dissipation parameters at contact surfaces, in which introducing a small error results in an accumulated error in the entire solution procedure. A solution for an unilateral contact problem with friction was proposed by Hlaváček and Nedoma [9, 10] in thermo-elasticity problems. It is usually permissible to treat the thermo-coupling problems with a partially uncoupled approach, particularly in the absence of plasticity. As a result, the augmented-Lagrange method can be applied on the basis of node-to-surface contact algorithm for non-matching meshes to impose the contact constraints of deformations, while the thermal contact resistance (TCR) can be enforced for the perfect/imperfect thermal constraints in the normal direction. This strategy makes the possibility of decomposition of coupled thermo-mechanical analysis into the purely thermal and mechanical simulations with individual boundary conditions. The interaction of thermal and mechanical problems can then be employed via the reciprocal effects of temperature on the stress fields, or the influence of contact normal forces on the thermal parameters.

There are a few research works reported in the literature regarding the thermo-mechanical analysis of contact problems; including a thermo-mechanical contact analysis by Oancea and Laursen [18] that contains the frictional thermal softening, pressure dependent heat conduction, and heat sinks on the contact surface; a contact pressure and temperature dependent thermal contact model with an operator split technique by de Saracibar [5] and Pantuso et al. [21]; a thermo-mechanical frictional contact algorithm by Xing and Makinouchi [27] for the multiple elastic–plastic bodies in finite deformation using the *R*-minimum strategy; an adaptive thermo-mechanical contact analysis by Rieger and Wriggers [24] that considers the contact heat flux and frictional dissipation; and a mortar approach for thermo-mechanical contact problems by Hueber and Wohlmuth [11] that takes into account the effects of frictional heating and thermal softening at the contact interface. A fact that has been usually ignored in the thermo-coupling analysis is the effect of velocity field in the thermal contact/impact problems, known as the convective heat transfer. This phenomenon is important in the analysis of the conventional thermo-mechanical problem, the thermal contact resistance, and the frictional dissipation treatment. Since the implementation of the standard Galerkin finite element method for the convection-diffusion problem results in numerical instability and a diffused solution, the Taylor-Galerkin method can be employed for the time dependent advection diffusion problem [6]. The numerical instability of thermo-dynamic analysis in frictional sliding systems was investigated by Morton [17] and Yi [29]. The main concept of this strategy is to utilize an improved approximation for the time derivative by including the higher order term of the Taylor series.

The main objective of this study is to present a thermo-dynamic modeling for large deformation contact–impact problem based on the Taylor-Galerkin method. The outline of this paper is as follows; In Section 2, the dynamic finite element formulation is presented based on the total Lagrangian approach with the hyperelastic material model. In Section 3, the heat transfer formulation is derived based on the Taylor-Galerkin approach and the relevant finite element formulation is demonstrated. In Section 4, the implementation of mechanical and thermal contact constraints is presented in contact-impact problems. In order to illustrate the capability of proposed computational algorithm, several numerical examples are presented in Section 5. Finally, Section 6 is devoted to conclusion remarks.

2. LARGE FINITE ELEMENT DEFORMATION FORMULATION

The main purpose of the non-linear dynamic finite element analysis involving large strain, large deformation and material nonlinearities is to establish an equation of virtual work and consequently to satisfy the equilibrium conditions between the internal and external forces. Considering the motion of particle in a fixed Cartesian coordinate, the differential equation for the dynamic equilibrium without damping can be expressed as

$$\frac{\partial \sigma_{ij}}{\partial x_j} - \rho \ddot{u}_i + b_i = 0 \tag{1}$$

where σ_{ij} is the Cauchy stress tensor, x the vector of current coordinates, ρ the mass per unit volume and b_i is referred to as the body force vector. In order to solve equation (1) numerically, the standard finite element procedure can be applied using the principle of virtual work, or displacement, to express the equilibrium of body in the unknown configuration as

$$\int_{\Omega} \boldsymbol{\sigma}^T \delta \boldsymbol{\varepsilon} \, d\Omega = - \int_{\Omega} \delta \boldsymbol{u}^T \rho \, \ddot{\boldsymbol{u}} \, d\Omega + \int_{\Omega} \delta \boldsymbol{u}^T \boldsymbol{b} \, d\Omega + \int_{\Gamma} \delta \boldsymbol{u}^T \boldsymbol{t} \, d\Gamma \tag{2}$$

where $\boldsymbol{\varepsilon}$ is the strain tensor usually known as the Almansi, or Euler strain tensor, and in the small deformation takes the form of engineering strain. In the above equation, $\boldsymbol{t}$ is the surface forces or the tractions applied on boundaries, in which for the simplicity it is assumed that its direction and magnitude are independent of any configuration and consequently the last integral includes the virtual work performed by the external forces.

In large deformations, the second Piola-Kirchhoff stress that is conjugate with the Green strain can be used as the stress measure. The virtual work expression can therefore be expressed as

$$\int_{\Omega^0} \boldsymbol{S}^T \delta \boldsymbol{E} \, d\Omega = - \int_{\Omega^0} \delta \boldsymbol{u}^T \rho^0 \ddot{\boldsymbol{u}} \, d\Omega + \int_{\Omega^0} \delta \boldsymbol{u}^T \boldsymbol{b}^0 \, d\Omega + \int_{\Gamma^0} \delta \boldsymbol{u}^T \boldsymbol{t} \, d\Gamma \tag{3}$$

where $\boldsymbol{E}$ and $\boldsymbol{S}$ denote the Green-Lagrange strain tensor and the second Piola-Kirchhoff stress tensor, respectively and '0' expresses that the variables are measured in the initial configuration as the total Lagrangian formulation is used. Following the standard finite element Galerkin discretization procedure, the linearization of the variational equation (3) in the framework of the Lagrangian description with independent approximations of $\boldsymbol{u}$ and $\ddot{\boldsymbol{u}}$ as $\boldsymbol{u} = \boldsymbol{N}\overline{\boldsymbol{u}}$ and $\ddot{\boldsymbol{u}} = \boldsymbol{N}\ddot{\overline{\boldsymbol{u}}}$ can be expressed as

$$\boldsymbol{\Psi}_{(\overline{\boldsymbol{u}}, \ddot{\overline{\boldsymbol{u}}})} = \int_{\Omega^0} \boldsymbol{B}^T \boldsymbol{F}^T \boldsymbol{S} \, d\Omega_0 + \int_{\Omega^0} \boldsymbol{N}^T \rho^0 \boldsymbol{N} d\Omega_0 \, \ddot{\overline{\boldsymbol{u}}} - \int_{\Omega^0} \boldsymbol{N}^T \boldsymbol{b}^0 \, d\Omega_0 - \int_{\Gamma^0} \boldsymbol{N}^T \boldsymbol{t} \, d\Gamma_0 = \boldsymbol{0} \tag{4}$$

where $\boldsymbol{\Psi}$ is a function of the displacement and acceleration and must be zero at each time step of the analysis, $\boldsymbol{N}$ is the vector of shape functions, $\boldsymbol{B}$ is the derivatives of shape functions with respect to initial coordinates defined as $B_{ji} = \partial N_i / \partial X_j$, and $\boldsymbol{F}$ is the deformation gradient defined by $F_{ij} = \partial x_i / \partial X_j$. In the first integration of equation (4), the stress field is dependent on the strain and consequently on the displacement due to large deformations and geometric nonlinearities [12].

In order to solve equation (4) in time domain, the generalized Newmark (GN_{22}) technique is applied for dynamic problems, and the unknown displacement and velocity fields are calculated using the variables of previous time step in the following form

$$\bar{\boldsymbol{u}}_{n+1} = \bar{\boldsymbol{u}}_n + \dot{\bar{\boldsymbol{u}}}_n \Delta t + \ddot{\bar{\boldsymbol{u}}}_n \frac{\Delta t^2}{2} + \beta(\ddot{\bar{\boldsymbol{u}}}_{n+1} - \ddot{\bar{\boldsymbol{u}}}_n)\frac{\Delta t^2}{2} \tag{5}$$

$$\dot{\bar{\boldsymbol{u}}}_{n+1} = \dot{\bar{\boldsymbol{u}}}_n + \ddot{\bar{\boldsymbol{u}}}_n \Delta t + \alpha(\ddot{\bar{\boldsymbol{u}}}_{n+1} - \ddot{\bar{\boldsymbol{u}}}_n)\Delta t \tag{6}$$

where the subscript n refers to the known values of variables at the last converged step of the analysis and $n+1$ refers to the unknown variables at the current configuration. The parameters α and β are the Newmark coefficients, in which for the unconditional stability $0 < \beta \leq \alpha < 1$. It can be easily shown from relation (5) that the acceleration can be obtained as

$$\ddot{\bar{\boldsymbol{u}}}_{n+1} = \frac{2(\bar{\boldsymbol{u}}_{n+1} + \hat{\boldsymbol{u}}_{n+1})}{\beta \Delta t^2} \tag{7}$$

where $\hat{\boldsymbol{u}}_{n+1}$ can be obtained using the known variables of time step n as

$$\hat{\boldsymbol{u}}_{n+1} = -\bar{\boldsymbol{u}}_n - \dot{\bar{\boldsymbol{u}}}_n \Delta t + \ddot{\bar{\boldsymbol{u}}}_n \frac{\Delta t^2}{2} + (\beta - 1)\ddot{\bar{\boldsymbol{u}}}_n \frac{\Delta t^2}{2} \tag{8}$$

Substituting relation (7) into the equilibrium equation (4) at time step $n+1$, it results in

$$\boldsymbol{\Psi}^{n+1}{}_{(\bar{\boldsymbol{u}})} = \int_{\Omega^0} \boldsymbol{B}^T \boldsymbol{F}^T \boldsymbol{S}\, d\Omega_0 + \int_{\Omega^0} \boldsymbol{N}^T \rho^0 \boldsymbol{N}\, d\Omega_0 \, \frac{2(\bar{\boldsymbol{u}}_{n+1} + \hat{\boldsymbol{u}}_{n+1})}{\beta \Delta t^2} - \boldsymbol{f}_{ext} = \boldsymbol{0} \tag{9}$$

where $\boldsymbol{f}_{ext}$ is referred as the external forces due to surface tractions and body forces. Applying the Newton-Raphson method to equation (9), the linearization of Lagrangian finite element formulation can be obtained as

$$\left(\int_{\Omega^0} \boldsymbol{B}^T \boldsymbol{S}\, \boldsymbol{B}\, d\Omega_0 + \int_{\Omega^0} \boldsymbol{B}^T \boldsymbol{F}^T \boldsymbol{D}\, \boldsymbol{F}\, \boldsymbol{B}\, d\Omega_0 + \frac{2}{\beta \Delta t^2} \int_{\Omega^0} \boldsymbol{N}^T \rho^0 \boldsymbol{N}\, d\Omega_0 \right) d\overline{\boldsymbol{u}} + \int_{\Omega^0} \boldsymbol{B}^T\, \boldsymbol{F}^T \boldsymbol{S}\, d\Omega_0 + \frac{2(\overline{\boldsymbol{u}}_{n+1} + \widehat{\boldsymbol{u}}_{n+1})}{\beta \Delta t^2} \int_{\Omega^0} \boldsymbol{N}^T \rho^0 \boldsymbol{N}\, d\Omega_0 - \boldsymbol{f}_{ext} = \boldsymbol{0} \tag{10}$$

where $\boldsymbol{D}$ is the 3×3 material property matrix of the isotropic homogenous material where its components are obtained by differentiating from the constitutive relationship between the second Piola-Kirchhoff stress and Green-Lagrange strain. There are various material models introduced in the literature to describe the constitutive relation from which the Mooney-Rivilin and Neo-Hookean models are appropriate for rubberlike materials undergoing moderately large deformations due to the large strains. In equation (10), the tangential stiffness matrix, mass matrix and load vectors are defined as

$$\begin{aligned} \boldsymbol{K}_c &= \int_{\Omega^0} \boldsymbol{B}^T \boldsymbol{S}\, \boldsymbol{B}\, d\Omega_0 \\ \boldsymbol{K}_s &= \int_{\Omega^0} \boldsymbol{B}^T \boldsymbol{F}^T \boldsymbol{D}\, \boldsymbol{F}\, \boldsymbol{B}\, d\Omega_0 \\ \boldsymbol{M} &= \int_{\Omega^0} \boldsymbol{N}^T \rho^0 \boldsymbol{N}\, d\Omega_0 \\ \boldsymbol{f}_{int} &= \int_{\Omega^0} \boldsymbol{B}^T\, \boldsymbol{F}^T \boldsymbol{S}\, d\Omega_0 \\ \boldsymbol{f}_{ext} &= \int_{\Omega^0} \boldsymbol{N}^T \boldsymbol{b}^0\, d\Omega_0 + \int_{\Gamma^0} \boldsymbol{N}^T \boldsymbol{t}\, d\Gamma_0 \end{aligned} \tag{11}$$

where $\boldsymbol{K}_c$ is the stiffness matrix for large deformation, $\boldsymbol{K}_s$ is the stress (or geometric) stiffness matrix, $\boldsymbol{M}$ is the mass matrix, $\boldsymbol{f}_{int}$ is the equivalent load vector due to stresses in the current configuration, and $\boldsymbol{f}_{ext}$ is the equivalent load vector due to surface loading and body forces. Finally, equation (10) can be simplified as $\boldsymbol{K}\, d\overline{\boldsymbol{u}} = \boldsymbol{f}$, with $\boldsymbol{K} = \boldsymbol{K}_c + \boldsymbol{K}_s + \frac{2}{\beta \Delta t^2} \boldsymbol{M}$ and $\boldsymbol{f} = \boldsymbol{f}_{ext} - \boldsymbol{f}_{int} - \frac{2(\overline{u}_{n+1} + \widehat{u}_{n+1})}{\beta \Delta t^2} \boldsymbol{M}$.

2.1 The temperature–dependent FE formulation

In order to incorporate the effect of temperature into the deformation and stress fields, the effect of thermal changes must be taken into the energy function of the isotropic hyper-elastic material model based on the thermal gradient and heat transfer analysis that leads to a non-isothermal energy function. The thermo-mechanical analysis is performed using the nonlinear mechanical modeling and heat transfer analysis. The nonlinear thermo-mechanical analysis can be carried out based on the free strain energy density function for the hyper-elastic models, such as the compressible Neo-Hookean or Mooney-Rivilin model, by decomposing the strain energy function into an effective strain energy function or elastic energy function and a function depending purely on a temperature. The strain energy density function for the compressible Neo-Hookean material can be expressed as

$$\psi_{(\boldsymbol{C}^e,\theta)} = \frac{1}{2}\lambda\left(ln(J^e)\right)^2 - \mu\, ln(J^e) + \frac{1}{2}\mu\,(Tr(\boldsymbol{C}^e) - 3) + h(T) \tag{12}$$

where $J^e = \det \boldsymbol{F}^e$, with $\boldsymbol{F}^e$ denoting the temperature-free deformation gradient obtained by decomposing the deformation gradient $\boldsymbol{F}$ into the effective stress related part of the deformation gradient $\boldsymbol{F}^e$ and the thermal deformation tensor $\boldsymbol{F}^\theta$ as

$$\boldsymbol{F} = \boldsymbol{F}^\theta \boldsymbol{F}^e \tag{13}$$

and $\boldsymbol{C}^e$ is the effective left Cauchy tensor defined as

$$\boldsymbol{C}^e = \boldsymbol{F}^{e^T} \boldsymbol{F}^e \tag{14}$$

in which the constitutive equation for the second Piola-Kirchhoff stress can be obtained by differentiating the energy function with respect to the effective left Cauchy tensor as

$$\boldsymbol{S} = 2\frac{\partial \psi}{\partial \boldsymbol{C}^e} \tag{15}$$

The main concept of above issue is that no stresses are produced by the free expansion due to the changes of temperature. In the case of isotropic temperature-dependent material behavior, the free expansion due to the changes of temperature is volumetric, and the thermal deformation tensor can be written as

$$\boldsymbol{F}^\theta = \gamma_{(T)} \boldsymbol{I} \tag{16}$$

where $\gamma_{(T)} = e^{\alpha T}$, with α denoting the temperature independent thermal expansion coefficient, $T = \theta - \theta_0$ is the changes of temperature with respect to the initial temperature of the particular region of the particle, and $\boldsymbol{I}$ is the identity tensor.

Since the thermal deformation tensor $\boldsymbol{F}^\theta$ is the stress-free part of the deformation gradient which contains both the free thermal expansion and deformation, the values of stresses depend merely on the effective stress related part of deformation gradient $\boldsymbol{F}^e$, which can be simply obtained by multiplication of the inverse of $\boldsymbol{F}^\theta$ by $\boldsymbol{F}$. In this manner, the effective symmetric left Cauchy tensor and the effective deformation gradient determinant defined in equation (14) can be obtained as

$$\begin{aligned} \boldsymbol{F}^e &= \left(\boldsymbol{F}^\theta\right)^{-1}\boldsymbol{F} = \frac{1}{\gamma_{(T)}}\boldsymbol{F} \\ J^e &= \det(\boldsymbol{F}^e) = \frac{1}{{\gamma_{(T)}}^3}\det(\boldsymbol{F}) = \frac{1}{{\gamma_{(T)}}^3}J \\ \boldsymbol{C}^e &= (\boldsymbol{F}^e)^T\boldsymbol{F}^e = \frac{1}{{\gamma_{(T)}}^2}\boldsymbol{C} \end{aligned} \tag{17}$$

The second Piola-Kirchhoff stress defined in the large deformation stiffness matrix $\boldsymbol{K}_c$ and the internal force $\boldsymbol{f}_{int}$ in relations (11) can be obtained using equation (15). In relation (11), the constitutive elasticity tensor $\boldsymbol{D}$ can be calculated by twice differentiating the effective energy function with respect to $\boldsymbol{C}^e$ and, the Green-Lagrange strain measurement that takes part in the geometric stiffness matrix $\boldsymbol{K}_s$ can be obtained from the total deformation gradient as

$$\boldsymbol{E} = \frac{1}{2}(\boldsymbol{F}^T\boldsymbol{F} - \boldsymbol{I}) \tag{18}$$

This procedure leads to a nonlinear strategy that deals with the effect of temperature changes on the deformation and stress fields through the Newton-Raphson procedure.

3. THE CONVECTION–DIFFUSION HEAT TRANSFER ANALYSIS

In order to perform the heat transfer analysis of convection–diffusion problem, the Taylor-Galerkin technique is employed here. Considering the motion of a mobile solid in a fixed Cartesian coordinate, the governing heat transfer equation can be written as

$$\rho c\left(\frac{\partial T}{\partial t} + \boldsymbol{V}.\boldsymbol{\nabla}T\right) = \boldsymbol{\nabla}.(\boldsymbol{k}\,\boldsymbol{\nabla}T) + Q \tag{19}$$

where T is the temperature field, ρ is the density of the medium, c is the specific heat parameter, $\boldsymbol{\nabla}$ denotes the gradient operator, $\boldsymbol{V} = [\dot{u}, \dot{v}]$ is the vector of constant velocity, $\boldsymbol{k}$ is the thermal conductivity tensor which may vary in space, and Q is the heat source. In above equation, $\boldsymbol{k}\,\boldsymbol{\nabla}T$ is a substitution for the heat flux q according to the Fourier law. Equation (19) is a highly nonlinear equation where the term containing $\boldsymbol{V}$ makes an unsteady condition.

The numerical solution of the convection–diffusion equation (19) by the standard Galerkin finite element method results in a diffused solution that can be related to the Peclet number, i.e. the proportion of the convection to diffusion effects. There are several approaches proposed by researchers for the time discretization of the purely diffusion equation, such as the backward/forward difference and the Crank-Nicolson schemes, however – they cannot be directly applied to the convection–diffusion problems. In fact, the result will not converge particularly when the convection term is dominant. The Taylor-

Galerkin technique is an efficient approach proposed in the literature to overcome this problem by adding an artificial diffusion to the existing diffusion, which is dependent on the thermal conductivity [25]. In order to apply the Taylor-Galerkin technique to the convection–diffusion equation, the time discretization of temperature field is written as

$$\frac{T^{n+1}-T^{n}}{\Delta t}=\frac{\partial T}{\partial t}+\frac{1}{2}\Delta t\frac{\partial^{2}T}{\partial t^{2}}+O(\Delta t^{2}) \tag{20}$$

where $\partial T/\partial t$ and $\partial^2 T/\partial t^2$ denote the first and second time derivatives of temperature field, respectively. To obtain the second time derivative of temperature, taking the time derivative from equation (19), results in

$$\rho c\left(\frac{\partial^{2}T}{\partial t^{2}}+\boldsymbol{V}.\boldsymbol{\nabla}\frac{\partial T}{\partial t}\right)=\boldsymbol{k}\,\boldsymbol{\nabla}^{2}\frac{\partial T}{\partial t} \tag{21}$$

in which it is assumed that the heat conductivity tensor is constant and the heat source is negligible. By expanding equation (21) for the two-dimensional problem, we obtain

$$\rho c\frac{\partial^{2}T}{\partial t^{2}}=-\rho c\dot{u}\frac{\partial}{\partial x}\left(\frac{\partial T}{\partial t}\right)-\rho c\dot{v}\frac{\partial}{\partial y}\left(\frac{\partial T}{\partial t}\right)+k\left(\frac{\partial^{2}}{\partial x^{2}}+\frac{\partial^{2}}{\partial y^{2}}\right)\frac{\partial T}{\partial t} \tag{22}$$

By combining equations (19) and (22) and removing the higher-order terms related to the third spatial derivatives, the second time derivative of temperature can then be obtained as

$$\frac{\partial^{2}T}{\partial t^{2}}=\dot{u}^{2}\frac{\partial^{2}T}{\partial x^{2}}+2\dot{u}\dot{v}\frac{\partial^{2}T}{\partial x\partial y}+\dot{v}^{2}\frac{\partial^{2}T}{\partial y^{2}}+\left(\frac{k}{\rho c}\right)\frac{\partial T}{\partial t} \tag{23}$$

Substituting the first and second time derivatives of temperature into the time discretization of temperature (20), yields the semi-discrete equation as

$$\begin{aligned}\frac{T^{n+1}-T^{n}}{\Delta t}=&\left[-\left(u\frac{\partial}{\partial x}+v\frac{\partial}{\partial y}\right)+\left(\frac{k}{\rho c}\right)\left(\frac{\partial^{2}}{\partial x^{2}}+\frac{\partial^{2}}{\partial y^{2}}\right)+u^{2}\frac{\partial^{2}}{\partial x^{2}}+2uv\frac{\partial^{2}}{\partial x\partial y}\right.\\&\left.+v^{2}\frac{\partial^{2}}{\partial y^{2}}\right]T^{n}+\left(\frac{k}{\rho c}\right)\left(\frac{\partial^{2}}{\partial x^{2}}+\frac{\partial^{2}}{\partial y^{2}}\right)\left(\frac{T^{n+1}-T^{n}}{\Delta t}\right)\end{aligned} \tag{24}$$

Following the standard finite element procedure, the linearization of the weak form of equation (24) with independent approximations of ${T^n}_{(x,y)}$ as $\boldsymbol{T}^n=\boldsymbol{N}\overline{\boldsymbol{T}}^n$ can be obtained as

$$\left(\frac{1}{\Delta t}\boldsymbol{C}+\frac{1}{2}\boldsymbol{H}\right)T^{n+1}=\left(\frac{1}{\Delta t}\boldsymbol{C}-\frac{1}{2}\boldsymbol{H}-\boldsymbol{C}_{a}+\boldsymbol{C}_{b}\right)T^{n}+\boldsymbol{g} \tag{25}$$

Where

$$\begin{aligned} \boldsymbol{H} &= \int_{\Omega} \boldsymbol{B}^T k\, \boldsymbol{B}\, d\Omega + \int_{\Gamma} \boldsymbol{N}^T h_{ext}\, \boldsymbol{N}\, d\Gamma \\ \boldsymbol{C} &= \int_{\Omega} \boldsymbol{N}^T \rho c\, \boldsymbol{N}\, d\Omega \\ \boldsymbol{C}_a &= \int_{\Omega} \boldsymbol{N}^T \rho c\, \boldsymbol{V}\, \boldsymbol{B}\, d\Omega \\ \boldsymbol{C}_b &= \frac{\Delta t}{2} \int_{\Omega} \boldsymbol{N}^T \boldsymbol{V}^T \rho c\, \boldsymbol{V}\, \boldsymbol{N}\, d\Omega \\ \boldsymbol{g} &= \int_{\Gamma} \boldsymbol{N}^T\, h_{ext}\, T_{\infty}\, d\Gamma \end{aligned} \tag{26}$$

in which the second integration of conductivity matrix $\boldsymbol{H}$ and the integration of thermal loading vector $\boldsymbol{g}$ can be obtained using the Neumann boundary condition at the surfaces subjected to the natural convection with the constant convection coefficient $h_{ext}(\mathrm{W}/(^{\mathrm{o}}\mathrm{C}.\mathrm{m}^2))$. It implies that the heat flux conducted to a body due to the heat conductive surfaces is obtained by $q = h_{ext}(T_{\infty} - T_{\mathrm{s}})$, with T_{∞} and T_s denoting the temperature of environment and body surface, respectively.

4. MODELING OF MECHANICAL AND THERMAL CONTACT CONSTRAINTS

In the thermo-mechanical contact problem, both mechanical and thermal aspects must be taken into account at the contact surface between two bodies. Consider a system of two deformable bodies known as the master and slave bodies, there are two sets of constraints to be enforced on contacting surfaces. The first set is related to mechanical constraints, which is generally categorized into the impenetrability and frictional constraints, and state that there is no inter-penetration between two bodies at the contact surface [13]. The impenetrability and frictional constraints can be modeled according to the normal and tangential relative displacements between two bodies in the contact zone, which is directly stated in terms of stick/slip conventional friction laws. The second set is concerned with the thermal constraints, which is related to the heat conduction condition and the heat generation due to the dissipation and frictional slipping. In what follows, the mechanical contact constraints are modeled using the augmented-Lagrangian technique, and the thermal contact constraints are presented in the next section.

In order to enforce the impenetrability contact condition, the normal distance function g_N and the normal contact force λ_N are introduced at the contact surface with the following condition $\mathrm{g}_N \geq 0$ and $\lambda_N \leq 0$, where g_N is the gap between two bodies at the contact surface which is negative in the case of penetration. According to the node-to-segment contact algorithm, the gap function g_N is referred to the normal or closest distance between a point

on the slave body $\boldsymbol{x}_s$ to its projection point $\bar{\boldsymbol{x}}_s$ on the master segment (1)–(2) defined by nodal coordinates $\boldsymbol{x}_m^1$ and $\boldsymbol{x}_m^2$, respectively, which can be simply obtained by taking the inner product of the normal unit vector $\boldsymbol{n}$ with the relative distance defined as

$$\mathrm{g}_N = \|\boldsymbol{x}_s - \bar{\boldsymbol{x}}_s\| = (\boldsymbol{x}_s - \boldsymbol{x}_m^1)^T \boldsymbol{n} \tag{27}$$

where

$$\begin{gathered} \bar{\boldsymbol{x}}_s = \boldsymbol{x}_m^1 + (\boldsymbol{x}_m^2 - \boldsymbol{x}_m^1)\xi \\ \boldsymbol{n} = \boldsymbol{e}_3 \times \boldsymbol{t} \end{gathered} \tag{28}$$

where $\xi = (\boldsymbol{x}_s - \boldsymbol{x}_m^1)^T \boldsymbol{t}$ is the dimensionless surface coordinate along the master surface and $\boldsymbol{t}$ is the normalized tangent vector along the master segment which is defined by

$$\boldsymbol{t} = (\boldsymbol{x}_m^2 - \boldsymbol{x}_m^1)/\|\boldsymbol{x}_m^2 - \boldsymbol{x}_m^1\| = (\boldsymbol{x}_m^2 - \boldsymbol{x}_m^1)/l \tag{29}$$

Similarly, the tangential gap between the slave node at the contact surface and the master segment can be defined by $\mathrm{g}_T = (\xi - \xi_0) l_0$. Different strategies can be used to define the tangential gap g_T, however, all these approaches lead to a non-symmetric tangential stiffness matrix.

Applying the augmented-Lagrangian technique for the implementation of contact constraints, the potential energy of contact between two bodies can be written as

$$\Pi_c = \frac{1}{2}\alpha_n (g_N)^2 + \lambda_N g_N + \gamma \left[\frac{1}{2}\alpha_T (g_T)^2 + \lambda_T g_T\right] + (1-\gamma) f_T g_T \tag{30}$$

where α_n and α_T are referred to the stiffness of springs imposed at the normal and tangential directions of contact surface and, λ_N and λ_T are the Lagrange-multipliers that represent the contact forces in the normal and tangential directions, respectively. The third and fourth terms in the above expression govern the sliding behavior between two bodies. Parameter γ is used to switch between the stick behavior where the relative velocity is zero ($\gamma = 1$) and the slip behavior where the relative velocity is non-zero ($\gamma = 0$). In the sticking behavior, the strain energy related to the tangential spring imposed at the contact surface represent the tangential forces known as the tangential Lagrange multipliers; while in the slipping behavior, the tangential relative movements are not restricted and the tangential forces are determined by $f_T = \mu N$ according to the constitutive law of friction, where the friction coefficient is mostly force independent and the normal force N can be replaced by λ_N.

The potential energy (30) can be minimized by taking derivative with respect to displacement as

$$\delta\Pi_c = [\alpha_n \mathrm{g}_N + \lambda_N]\delta\mathrm{g}_N + [\gamma\alpha_T \mathrm{g}_T + \gamma\lambda_T + (1-\gamma)f_T]\delta\mathrm{g}_T \tag{31}$$

where the variation of gap functions $\delta\mathrm{g}_N$ and $\delta\mathrm{g}_T$ can be directly related to the variation of displacement fields as

$$\begin{aligned} \delta\mathrm{g}_N &= \boldsymbol{n}^T \boldsymbol{N}_\xi \delta\boldsymbol{u} = \boldsymbol{N}_n \delta\boldsymbol{u} \\ \delta\mathrm{g}_T &= \frac{l_0}{l_n}\left[\boldsymbol{t}\boldsymbol{N}_\xi - \boldsymbol{I}_n \mathrm{g}_N / l_n\right]\delta\boldsymbol{u} = \frac{l_0}{l_n}[\boldsymbol{N}_t - \boldsymbol{I}_n \mathrm{g}_N / l_n]\delta\boldsymbol{u} \end{aligned} \tag{32}$$

where $\boldsymbol{I}_n = \partial \boldsymbol{N}_n / \partial\xi$ and the contact shape function $\boldsymbol{N}_\xi$ is defined as

$$\boldsymbol{N}_\xi = \begin{bmatrix} 1 & 0 & -(1-\xi) & 0 & -\xi & 0 \\ 0 & 1 & 0 & -(1-\xi) & 0 & -\xi \end{bmatrix} \tag{33}$$

Further details are presented here for the stick case; the implementation of the slip case can be performed in a similar manner. Substituting relations (32) into (31), the variation of the potential energy can be written in terms of the variation of displacement field as

$$\begin{aligned} \delta\Pi_c &= \left\{(\alpha_n \mathrm{g}_N + \lambda_N)\boldsymbol{n}^T\boldsymbol{N}_\xi + (\alpha_t \mathrm{g}_T + \lambda_T)\frac{l_0}{l_n}\left[\boldsymbol{t}\boldsymbol{N}_\xi - \boldsymbol{n}^T\boldsymbol{N}_\xi \mathrm{g}_N / l_n\right]\right\}\delta\boldsymbol{u} \\ &\equiv \frac{\partial\Pi_c}{\partial\boldsymbol{u}}\delta\boldsymbol{u} = \psi_c^T \delta\boldsymbol{u} \end{aligned} \tag{34}$$

where ψ_c is referred to the contact-related internal forces. It is worth mentioning that the Lagrange-multipliers λ_N and λ_T in the variation of potential energy are functions of displacement and can be obtained in an iterative manner using the Newton-Raphson procedure.

Finally, the minimization of the potential energy (34) leads to the contact stiffness matrix $\boldsymbol{K}_c$, which is a symmetric matrix and can be defined based on the normal and tangential contact stiffness matrices $\boldsymbol{K}_N$ and $\boldsymbol{K}_T$ as

$$\begin{aligned} \boldsymbol{K}_N &= {\boldsymbol{N}_n}^T \alpha_n \boldsymbol{N}_n + \alpha_n \mathrm{g}_N \left[{\boldsymbol{I}_n}^T \boldsymbol{N}_t + {\boldsymbol{N}_t}^T \boldsymbol{I}_n\right]/l_n - \alpha_n {\mathrm{g}_N}^2 {\boldsymbol{I}_n}^T \boldsymbol{I}_n / {l_n}^2 \\ \boldsymbol{K}_T &= {\widehat{\boldsymbol{N}}_t}^T \alpha_t \widehat{\boldsymbol{N}}_t + \widehat{\boldsymbol{K}}_T + {\widehat{\boldsymbol{K}}_T}^T \end{aligned} \tag{35}$$

where

$$\begin{aligned} \widehat{\boldsymbol{N}}_t &= \frac{l_0}{l_n}\left[\boldsymbol{N}_t - \boldsymbol{I}_\xi \mathrm{g}_N / l_n\right] \\ \widehat{\boldsymbol{K}}_T &= \alpha_t \mathrm{g}_T (l_0/l_n)\left[{\boldsymbol{N}_n}^T \boldsymbol{I}_n + {\boldsymbol{N}_t}^T \boldsymbol{I}_t - (2\mathrm{g}_N/l_n){\boldsymbol{I}_n}^T \boldsymbol{I}_t\right] \end{aligned} \tag{36}$$

The contact stiffness matrices and internal force vectors derived above for sticking behavior will be assembled in the total stiffness matrix and force vector, and the system of

equation will then be solved at each time increment. The value of gap function will be checked not to be positive according to a pre-defined tolerance, and the Lagrange multipliers will be updated according to the calculated gap function as $\lambda_{new} = \lambda_{old} + \alpha g$ for each contact node-segment pairs.

4.1 The thermal contact constraints

Consider two deformable bodies in contact, the governing equations of heat transfer analysis for each body have been presented in preceding sections. In this section, the thermal behavior at the contact surface is discussed and the implementation of thermal contact constraints is described. There are two important issues that must be addressed in the thermal behavior of contact bodies; one is the heat flux at the contact surface and the other is the heat generation due to the friction and energy dissipation. Basically, there are three approaches to transmit the heat from one surface to another; firstly the heat conductance due to the radiation released from the vacuum space left between perfectly in-contact zones, secondly the heat conductance through the gas contained in micro-cavities, and lastly the heat conductance through the spots where two deformable bodies are purely in contact. However, in the case of the spot heat conductance, the two former approaches can be neglected.

Following the node-to-segment contact algorithm and considering an arbitrary point at the slave body that comes in contact with the master body, the heat flux q_N^s conducted across the slave body at the contact surface can be expressed by

$$q_N^s = (\theta_s - \hat{\theta}_s)/R_{(\Delta\theta,\lambda_N)} \tag{37}$$

where θ_s is the temperature assigned to the slave node and $\hat{\theta}_s$ is the temperature of the projected closest point of the slave node to the master segment that can be expressed using the values of two relevant nodes of the segment by $\hat{\theta}_s = \theta_m^1 + (\theta_m^2 - \theta_m^1)\xi$. In the above relation, R is the thermal contact resistant coefficient, and is defined to guarantee the heat flux continuity between two surfaces. This experimental coefficient depends on the temperature of the surface and the contact pressure, but in moderate temperature fields it can be assumed to be merely pressure dependent; so it cannot add any nonlinearity to the thermal analysis. In order to satisfy the continuity of heat conductance at the contact surface it is assumed that the rate of heat conductance across the slave surface is equal to that of the master surface and for each node of the master segment the heat conductance quota can be calculated using the zero moment equilibrium as

$$\sum q_N = q_N^s + {q_N}_m^1 + {q_N}_m^2 = 0 \tag{38}$$

where ${q_N}_m^1 = -(1-\xi)q_N^s$ and ${q_N}_m^2 = -\xi q_N^s$. Substituting the expression $\hat{\theta}_s$ into relation (37) results in a set of three equations that can be solved simultaneously using the system of equations derived before for the rest of the bodies as

$$\boldsymbol{q}_N = \boldsymbol{N}_\xi{}^T \boldsymbol{N}_\xi \boldsymbol{\theta} / R_{(\lambda_N)} \tag{39}$$

where $\boldsymbol{N}_\xi = [1 \quad -(1-\xi) \quad -\xi]$ and $\boldsymbol{\theta} = [\theta_s \quad \theta_m^1 \quad \theta_m^2]$. It must be noted that these equations satisfy the heat conductance continuity rather than the temperature field continuity, however – the difference between temperatures of contact surfaces depends on the contact resistance coefficient. This issue will be investigated in details in the numerical examples.

The heat generation due to the friction produced between two surfaces can be modeled by introducing the heat flux generated during the process of relative slipping between two in-contact surfaces. It is assumed that the heat flux is a function of the normal pressure and the average temperature between two surfaces, nonetheless a merely pressure dependence can be assumed in a moderate thermal field. The relevant expression for the heat flux across the slave surface can be stated by

$$q_D^s = D_{(\lambda_N, \theta_{ave})} \delta g_T \tag{40}$$

An expression for the heat conduction across the master segment can be defined similar to the heat flux value assumed for the slave node by its projection along the master segment; so the heat flux value of the master segment nodes can be obtained using $q_N{}_m^1 = (1-\xi) q_D^s$ and $q_N{}_m^2 = \xi q_D^s$. In order to incorporate the effect of energy dissipation and heat generation on the temperature field and subsequently the stress field during the frictional contact process, the resulting tangent stiffness matrix is assembled with the global stiffness matrix to satisfy the heat conduction continuity and the heat flux force produced in the system.

5. NUMERICAL SIMULATION RESULTS

The main strategy for the numerical solution of thermo-mechanical problems is that the fully coupled system must be solved simultaneously to obtain the displacement and temperature fields. However, it may lead to the numerical instability since the condition number for the system of equations of the heat transfer analysis is different from that of the momentum equations. This may cause more iterations for the nonlinear solution procedure, or the system may not converge to a unique solution. So it is a common approach to uncouple the governing systems of momentum and heat transfer equations to account for the reciprocal influences of systems on each other at the end of solution. Furthermore, it makes possible to perform a static analysis for the momentum equation, such as the displacement control problem, while the heat transfer analysis can be carried out using a transient one, where the relevant solution is the time dependent and can be obtained by an appropriate dynamic strategy. According to the numerical procedure described above for the solution of uncoupled thermo-mechanical problems, a computational algorithm is applied based on the Newton-Raphson approach. For the time step n, the algorithm is performed as follows;

1) Initialize the values of displacement, velocity, acceleration and temperature fields as boundary conditions. Assign the slave nodes and master segments, and calculate the initial gap between two surfaces.

2) Evaluate the total tangential stiffness matrix and the residual force. The total stiffness matrix contains the stiffness matrix of the contact zone and that obtained for two continuum bodies. Also, the residual force consists of the thermal, internal, external and contact forces.

3) Solve the momentum equation based on the augmented Lagrangian technique, and determine the Lagrange multipliers as the normal and tangential forces. Obtain the normal gap between two surfaces that must be enforced to be zero iteratively. Compute the incremental nodal displacements and relevant velocities or accelerations. Check the convergence for the gap function, and continue the procedure until the convergence is obtained.

4) Check the convergence for the momentum equilibrium, and continue to stage (ii) if the solution is not converged.

5) Update the thermal contact resistance coefficients using the normal forces.

6) Perform the thermal analysis using the Taylor-Galerkin approach where the convection term cannot be neglected, or perform any conventional procedure for the purely diffusion based problems and update the temperature filed.

It must be noted that in the above computational algorithm the stiffness matrix and residual force are assumed to be constant at each iteration of the solution in order to obtain the values of Lagrange multiplier and gap function. The thermal analysis is performed after the mechanical analysis by updating the interface parameters, and checking the convergence of the overall system of equations. In what follows, the capability and robustness of the proposed computational algorithm are presented for various thermo-mechanical problems, including the heat generation due to the frictional contact produced between two bodies. The first three examples are chosen to illustrate the performance of proposed model in the simulation of thermo-mechanical contact problems; while in the last two examples, the performance of Taylor-Galerkin technique is presented in the coupled thermo-dynamic analysis where the effect of convection term is dominant.

5.1 Thermo-mechanical analysis of contact between two plates

The first example is chosen to verify the accuracy of proposed computational algorithm in modeling of prefect and imperfect thermal contact of deformable bodies. The problem consists of two homogenous isotropic square plates with the same material properties, as shown in Fig. 1, in which the effect of temperature changes is investigated on the stresses of deformable bodies. The finite element simulation is performed using 400 four-noded quadrilateral elements for the upper plate and 441 four-noded elements for the lower plate that leads to the non-matching meshes at the contact interface. Both plates are fixed at one end, where the bottom edge is subjected to the temperature of $T_1 = 273^{o}\text{K}$ and the top edge to the temperature of $T_2 = 373^{o}\text{K}$. The lateral free surfaces of two bodies are assumed to be thermally isolated while the remaining parts are subjected to a constant convection coefficient of $h_{ext} = 1100\ \text{W}/(^{o}\text{K}.\text{m}^2)$. The frictionless thermal contact is considered between two plates. The numerical modeling is performed by applying the normal penalty coefficient ten times higher than that of the elasticity modulus of plate. Two different pressure dependent thermal contact resistance, i.e. the semi-prefect and imperfect thermal contact conditions, are assumed as

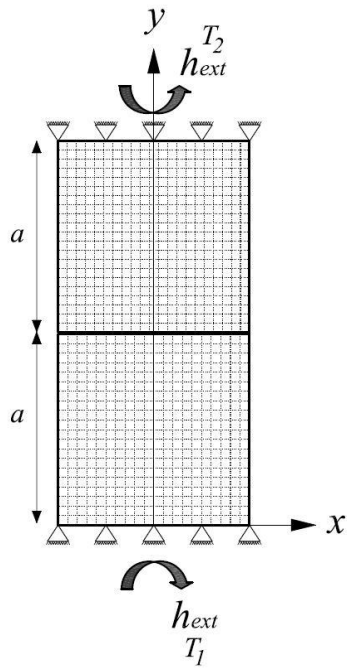

(a)

Elasticity module	$E = 2 \times 10^{11}$ Pa
Poisson ratio	$\nu = 0.3$
Thermal expansion	$\alpha = 2 \times 10^{-5}$ K^{-1}
Thermal conductivity	$k = 2 \times 10^{-5}$ W/m.K
Thermal capacity	$c = 2 \times 10^{-5}$ 1/K
Density	$\rho = 7.8 \times 10^{3}$ kg/m^3
a	0.25 m
T_1	273°K
T_2	373°K

(b)

Figure 1. Thermo-mechanical analysis of contact between two plates; a) The geometry, boundary condition and b) Material properties

$$R_1(\sigma_n) = 2.5e^{-0.01\sigma_n} \times 10^{-3} \tag{41}$$

$$R_2(\sigma_n) = 2.5e^{-0.01\sigma_n} \times 10^{-4} \tag{42}$$

where σ_n (MPa) is the contact pressure between two surfaces. In the heat transfer analysis, the transient dynamic analysis is performed with the time step of $\Delta t = 10$s, and the velocity is neglected since the top and bottom edges are fixed. As a result, a mechanical static analysis is performed for the momentum equation. The convergence tolerance is set to $1.0E-05$. In Fig. 2, the distributions of stress σ_y, stress σ_x and temperature contours are presented at the steady state condition for the semi-prefect contact condition. In Fig. 3, the distributions of temperature are plotted along *y*–direction at different time intervals in the case of semi-perfect thermal contact, i.e. $R_1(\sigma_n)$. Clearly, it can be seen that the steady state condition can be reached for the time interval greater than $6.0E+03$s. In Fig. 4, a comparison of temperature distribution along *y*–direction is performed between the perfect and imperfect conditions. Obviously, it can be observed that the proposed computational model can be efficiently used in modeling the coupled thermo-mechanical problem with prefect and imperfect thermal contact conditions.

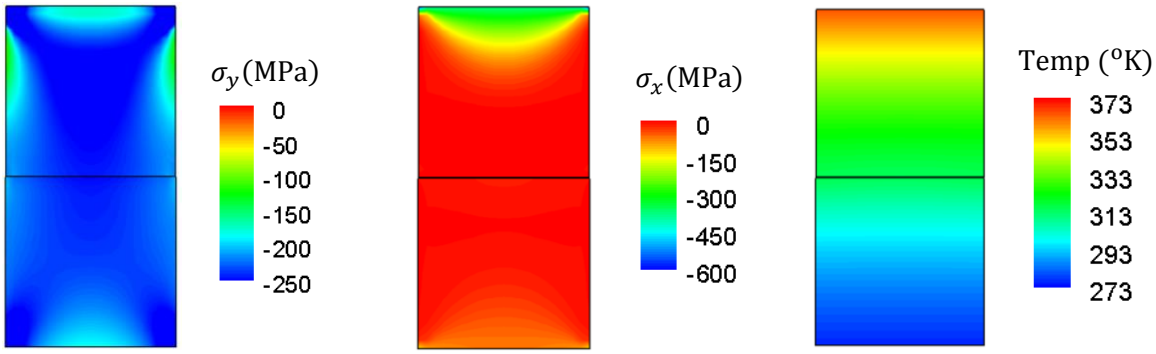

(a) (b) (c)

Figure 2. Thermo-mechanical analysis of contact between two plates; a) Stress σ_y contour, b) Stress σ_x contour (c) Temperature contour

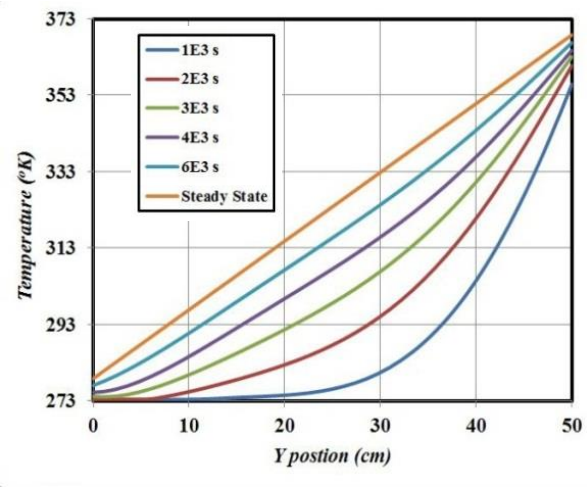

Figure 3. The temperature distribution along *y*–direction at different time intervals

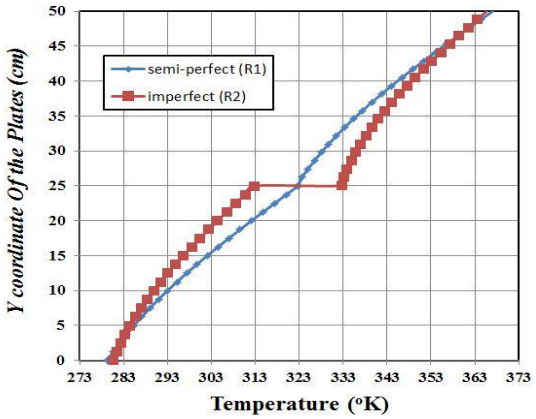

Figure 4. A comparison of the temperature distribution along *y*–direction between the semi-perfect (R_1) and imperfect (R_2) thermal contact conditions

5.2 Thermo-mechanical contact between a circular disc and a plate with hole

The second example deals with the thermo-mechanical analysis of contact between a circular disc and a plate with hole, as shown in Fig. 5. This example is chosen to illustrate the capability of proposed computational algorithm in large deformation problem with curved interfaces. All boundary surfaces are subjected to the natural convection, where the temperature for the outside the plate is set to 273^{o}K, inside the plate is 278^{o}K and outside the disk is set to 293^{o}K. The frictionless contact condition is assumed between two bodies that leads to no heat generation in the contact zone due to the relative tangential displacement at the contact surface. The thermal properties of the materials are similar to those of previous example, but the thermal resistance is 1000 times higher than that of previous example. The geometry, boundary condition and initial FE mesh are shown in Fig. 5. The system is modeled by increasing the prescribed vertical displacement at the circular disk up to 10 mm through the clamped nodes of the disk. The process is performed in 400 increments with a heat transfer analysis to reach the steady state condition at each step for both perfect and imperfect thermal contact conditions. The distributions of the temperature and normal stress σ_y contours are presented in Fig. 6 for various deformed configurations at the initial, half and final stages of the thermal and mechanical loadings. In Fig. 7, the variations of temperature with the normal stress are plotted at the lowest point of circular disc for the perfect (R_1) and imperfect (R_2) thermal contact conditions. It can be observed that the temperature declines as the circular disk moves down. This is concerned with the process of deformation at the contact surface and the increase of contact pressure during this process. This example clearly illustrates the efficiency of proposed computational algorithm in the thermo-mechanical problems undergoing large deformations.

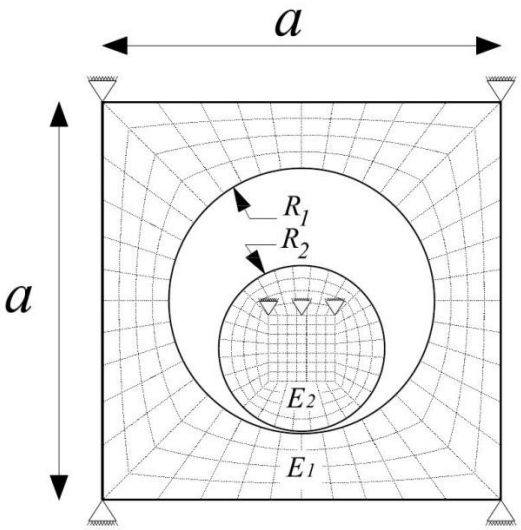

(a)

$E_1 = 2.08 \times 10^9$ N/m^2
$E_2 = 1.7 \times 10^5$ N/m^2
$\nu = 0.3$
$\alpha_N = 10E_1$
$R_1 = 0.08$ m
$R_2 = 0.05$ m
$a = 0.24$ m

(b)

Figure 5. The thermo-mechanical modeling of contact between a circular disc and a plate with hole; a) The geometry and boundary condition b) material properties

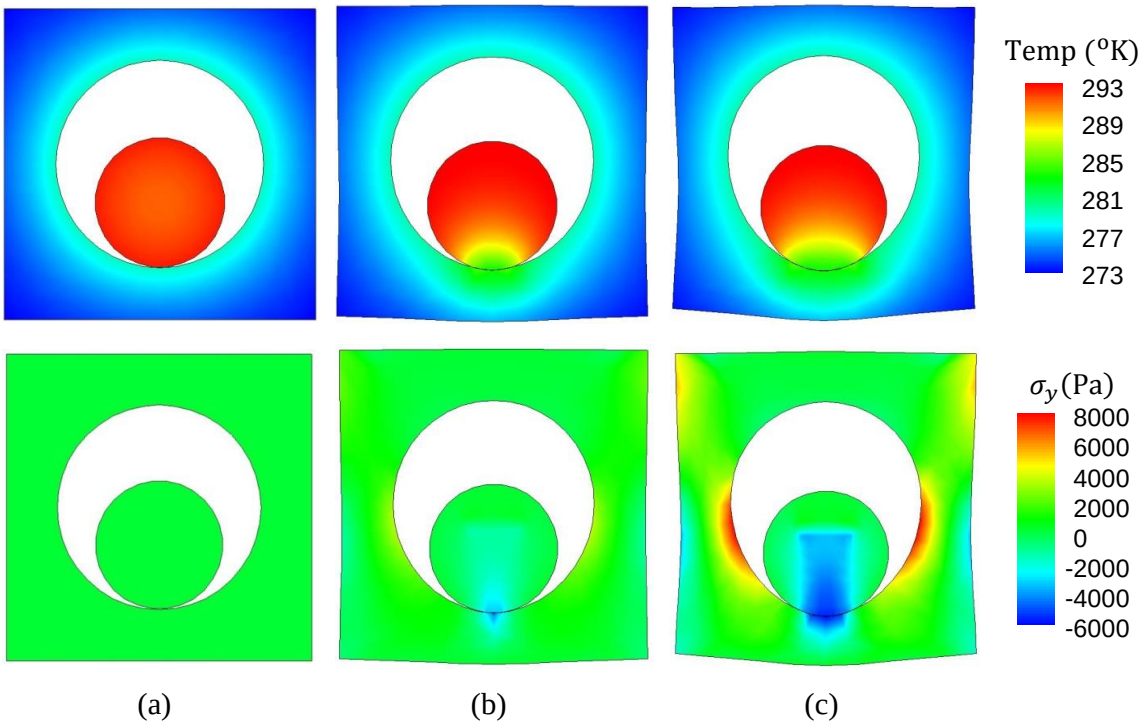

Figure 6. The contours of temperature and normal stress in the deformed configurations; a) the initial configuration, b) the half stage of loading, c) the final stage of thermal and mechanical loadings

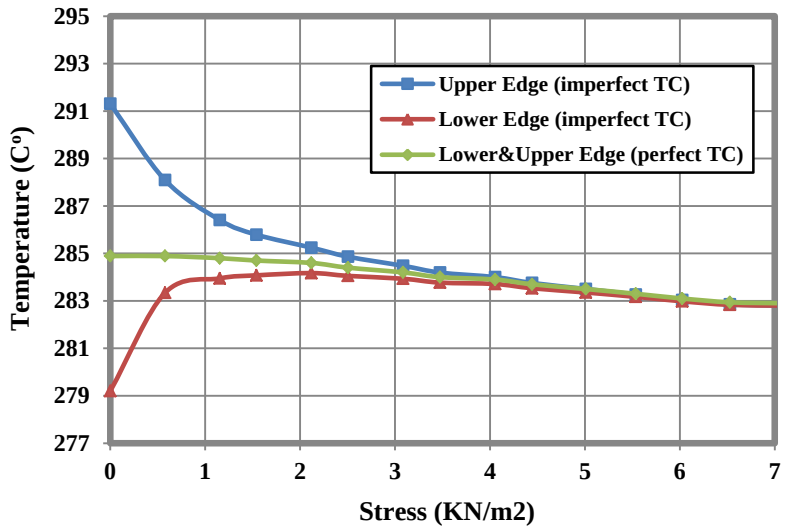

Figure 7. The variations of temperature with the normal stress at the lower point of circular disc for the perfect (R_1) and imperfect (R_2) thermal contact conditions

5.3 Heat generation due to frictional contact in pressing of a cylindrical plate

The next example is concerned with the heat generation mechanism due to the frictional dissipation. This example is chosen to illustrate the performance of proposed model in the thermo-mechanical analysis of heat generation due to frictional contact in pressing of a semi-cylindrical plate, as shown in Fig. 8. The problem consists of an elastic thick wall cylinder considered to be pressed under a semi-rigid rectangle plate. The prescribed displacement employed at the top rectangle plate leads to the relative tangential displacement at the contact interface, which causes the heat generation at this region. The horizontal movement of the upper plate is constrained by the lateral rollers and a prescribed displacement is applied at all nodal points of the upper surface in the vertical direction. The cylinder is statically constrained using a hinge and a roller. The upsetting process is performed in the plain stress condition by neglecting the inertia forces within the total time of 100s in the time interval of $\Delta t = 0.01\text{s}$. Both the semi-cylindrical plate and the semi-rigid rectangle plate are assumed to have the same thermal and mechanical properties, except the elasticity modules of rectangle plate which is 1000 times higher than that of the cylindrical plate. The frictional behavior of the system at the contact surface is modeled using a constant frictional coefficient of 0.3. The numerical simulation is performed using 270 four-noded quadrilateral elements for the rectangle plate and 600 four-noded elements for the cylindrical plate. Each free surface is assumed to be thermally isolated and the heat generation is modeled on the basis of frictional dissipation as the heat source at the contact surface. In Fig. 9, the distributions of normal stress and temperature contours are presented at various stages of upsetting process. This example exhibits the capability of proposed computational algorithm in modeling the frictional dissipation at the contact surface between two bodies in large deformations.

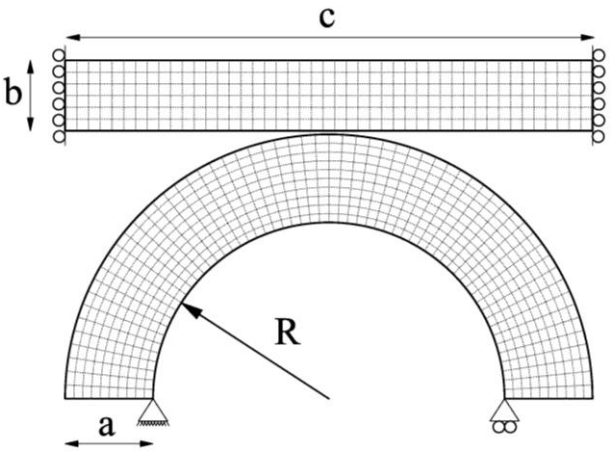

(a)

$E_1 = 2 \times 10^{11}\ \text{N/m}^2$
$E_2 = 2 \times 10^{7}\ \text{N/m}^2$
$\nu = 0.3$
$\alpha_N = 10E_1$
$R = 10\ \text{cm}$
$a = 5\ \text{cm}$
$b = 4\ \text{cm}$
$c = 3\ \text{cm}$

(b)

Figure 8. The thermo-mechanical analysis of heat generation due to frictional contact in pressing of a semi-cylindrical plate; a) The geometry, boundary condition and FE mesh, b) The material properties

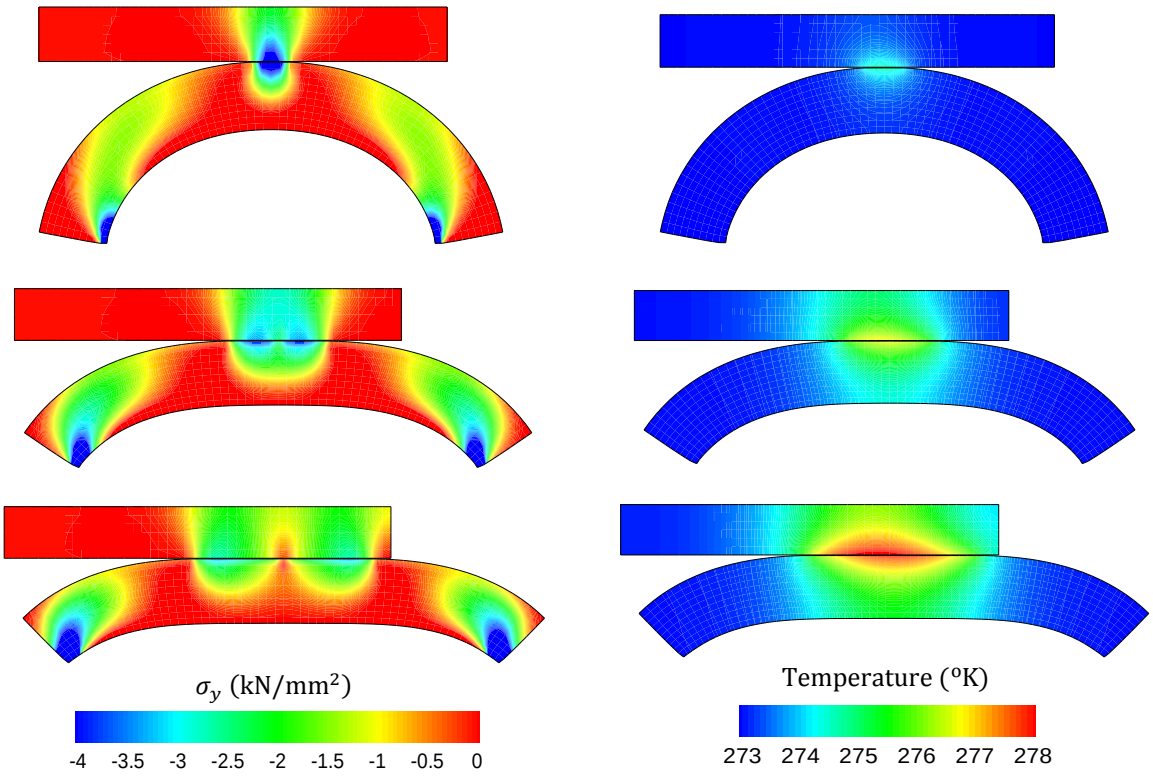

Figure 9. The distributions of the a) normal stress and b) temperature contours at various stages of pressing

5.4 Modeling of heat generation due to the slippery friction

The next example is chosen to illustrate the performance of Taylor-Galerkin technique in the thermo-dynamic analysis where the effect of convection term is important in the heat generation process due to the slippery friction between two deformable bodies. This example was originally modeled by Rieger and Wriggers [24], in which an elastic block was modeled to be sliding over a rectangular plate with the horizontal movement of 4 mm within the total time of 4 μs. In the simulation proposed in this reference, the effect of inertia forces in the momentum equation and the velocity term in the heat transfer analysis were ignored although the velocity of 1000 mm/s was reported in the heat transfer analysis. In the present study, the effect of convection term is incorporated by employing the Taylor-Galerkin technique into the thermo-dynamic analysis, and the results are compared with that obtained by the Crank-Nikolson scheme in the absence of convection term.

The system is modeled using two time-dependent loads applied on the top and left edges of the upper block, which leads to the maximum horizontal velocity of 12700 mm/s within the total time of 1 μs. Both bodies are made of aluminum with the material properties given in Table 1. The geometry, boundary conditions and initial FE mesh are shown in Fig. 10. The numerical simulation is performed using 120 four-noded quadrilateral elements for the

upper block and 350 elements for the lower body. The time step for numerical modeling is set to $\Delta t = 1E-6$s. In Fig. 11, a comparison of temperature distributions due to the slippery friction is performed between the case where the effect of artificial diffusion caused by the velocity term is considered in the proposed Taylor-Galerkin approach and the case where this effect is neglected. In Figs. 11(a–c), the temperature distributions are shown at different velocities where the effect of velocity is neglected in the heat transfer analysis using the Crank-Nikolson scheme. In Figs. 11(d–f), the temperature contours are presented at different velocities where the effect of velocity is taken into the heat transfer analysis using the Taylor-Galerkin technique. This example clearly presents the performance of Taylor-Galerkin technique in the thermo-dynamic analysis where the effect of convection term is important in the heat generation process.

Table 1: The aluminum material properties

Elasticity module	$E = 7 \times 10^4$ N/mm^2
Poisson ratio	$\nu = 0.3$
Thermal expansion coefficient	$\alpha = 2.386 \times 10^{-5}$ K^{-1}
Thermal conductivity	$k = 150$ N/s K
Thermal capacity	$c = 0.9 \times 10^9$ mm^2/s^{2}K
Density	$\rho = 2.7 \times 10^{-9}$ Ns^2/mm^{-4}
Thermal resistant coefficient	$h_{co} = 150$ N/s K

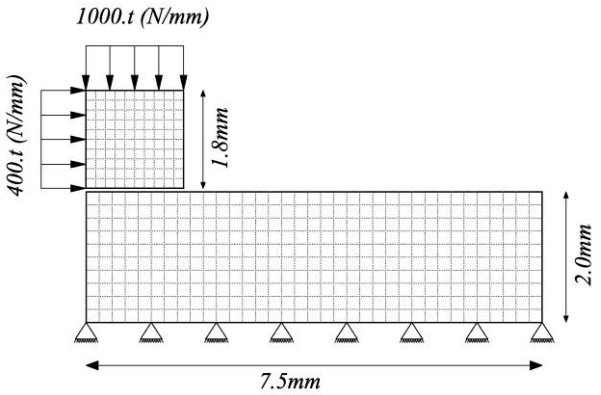

Figure 10. The thermo-dynamic modeling of heat generation due to the slippery friction between two deformable bodies; The geometry, boundary condition and FE modeling

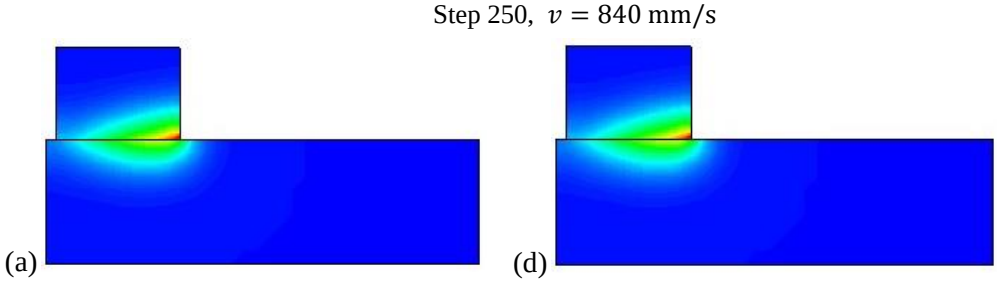

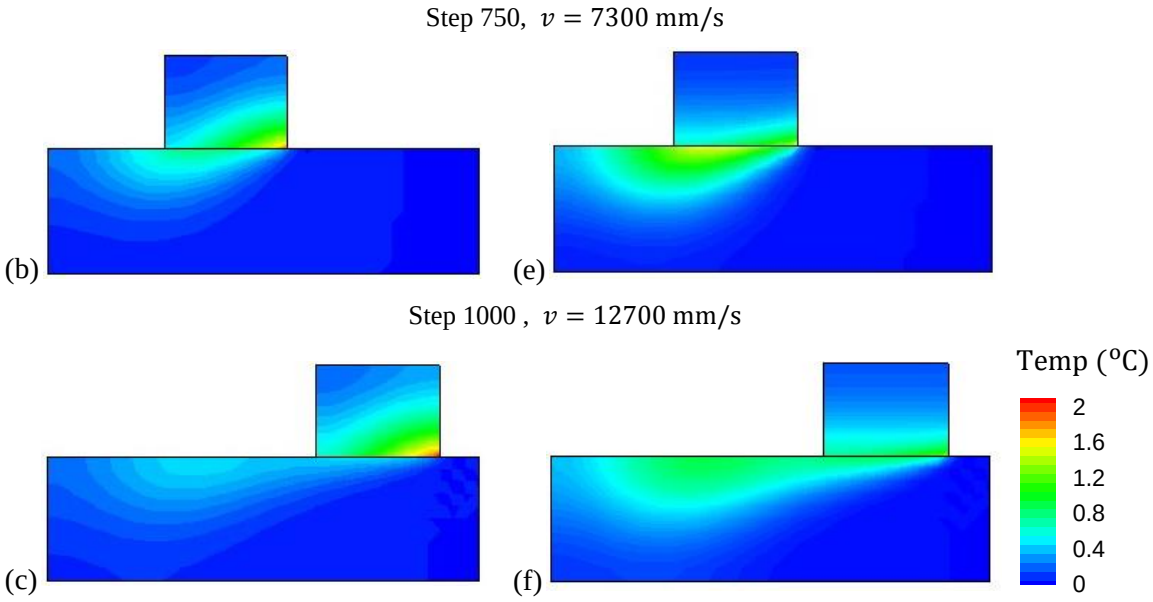

Figure 11. A comparison of temperature distribution due to the slippery friction between two deformable bodies; (a–c) the velocity is neglected in the heat transfer analysis (the Crank-Nikolson scheme), (d–f) the velocity is taken into account in the heat transfer analysis (the Taylor-Galerkin scheme)

5.5 Thermo-dynamic modeling of contact-impact of a ring to a rigid plate

The last example is chosen to illustrate the capability of proposed thermo-dynamic analysis in modeling the heat generation due to large deformation and frictional contact. The example presents the contact-impact of an elastic ring to a rigid plate, as shown in Fig. 12. The geometry, boundary conditions and the initial FE mesh is shown in this figure. Both the elastic ring and rigid plate are assumed to be made of the Neo-Hookian material with the material properties given as follows; the Young modules of $E = 2.0\text{E} + 5$, the mass density per unit volume of $\rho = 8.0\text{E} - 6$ and the thermal coefficient of $\alpha = k/\rho C = 1.0\text{E} + 3$. The ring is subjected to an initial velocity vector of $(8000, -8000)$ in all nodal points at the beginning of simulation. Both bodies have an initial zero temperature, and all free surfaces are assumed to be thermally isolated. The numerical simulation is performed using 160 four-noded quadrilateral elements for the ring and 90 elements for the rigid plate. The frictional behavior is modeled using the normal and tangential penalty parameters of $\alpha_N = \alpha_T = 10$, where the slipping friction coefficient is set to $\mu = 0.3$. The time step for numerical simulation is set to $\Delta t = 1E - 6\text{s}$.

The numerical modeling is performed in two different cases; firstly the effect of convection because of the velocity term in the heat transfer analysis is accounted by employing the Taylor-Galerkin approach, and secondly the effect of velocity in the heat transfer analysis is neglected by applying the Crank-Nikolson scheme. In Fig. 13, the distributions of normal stress σ_y contour are presented in the deformed configurations at different time steps. In Fig. 14, a comparison of temperature distributions is performed between the above two cases at different time steps. In Figs. 14(a–e), the temperature

distributions are shown at different time steps where the effect of velocity is neglected in the heat transfer analysis using the Crank-Nikolson scheme. In Figs. 14(f–j), the temperature contours are presented at different time steps where the effect of velocity is taken into the heat transfer analysis using the Taylor-Galerkin technique. This figure clearly presents the significance of velocity term in the heat transfer analysis, where the effect of artificial diffusion cannot be neglected on the temperature distribution. This example adequately illustrates the capability of proposed thermo-dynamic analysis in modeling of heat generation due to contact-impact problem.

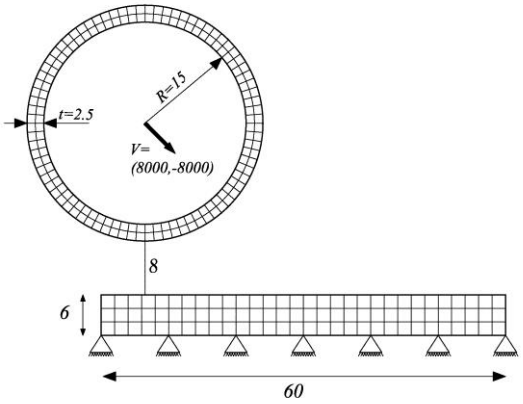

Figure 12. The thermo-dynamic modeling of heat generation due to the contact-impact of a ring to a rigid plate; The geometry, boundary condition and the initial FE mesh

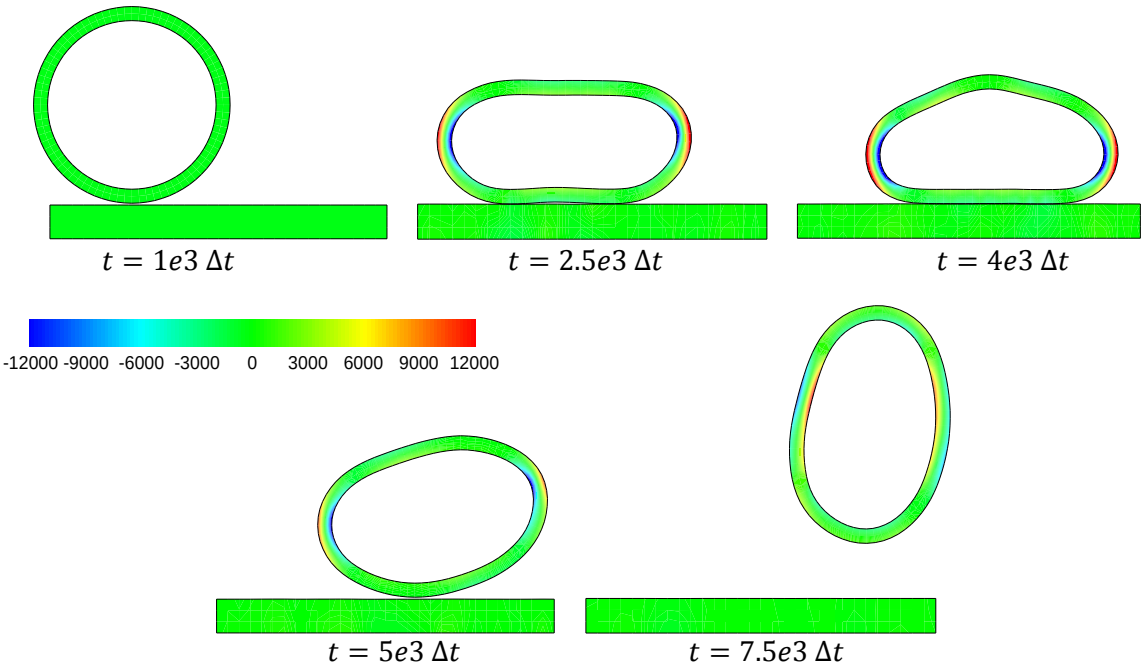

Figure 13. The deformed configuration and the distribution of normal stress σ_y contours at different time steps

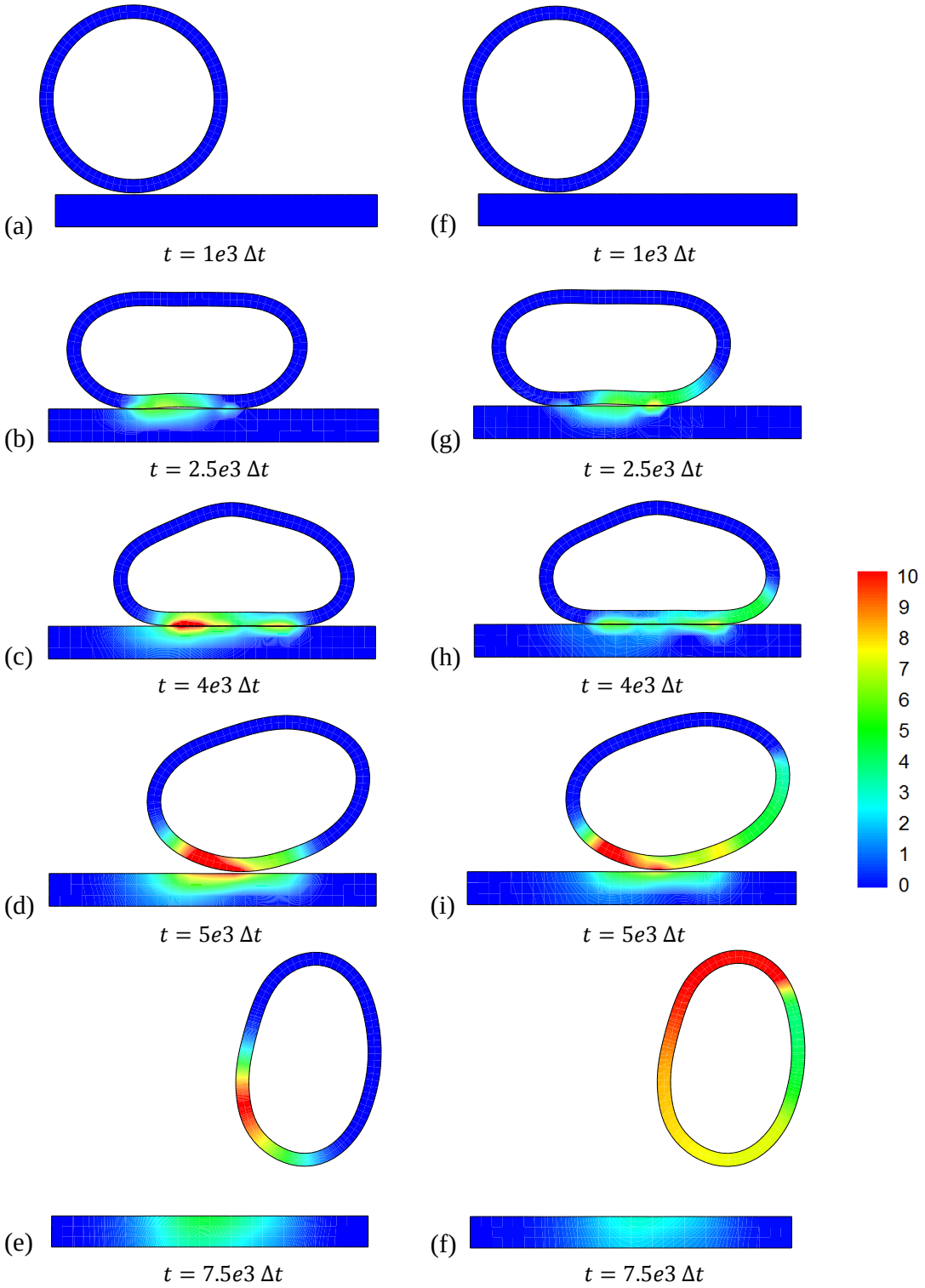

Figure 14. A comparison of temperature distribution; (a–e) the velocity is neglected (Crank-Nikolson method), (f–j) the velocity is taken into heat transfer analysis (Taylor-Galerkin method)

6. CONCLUSION

In the present paper, the thermo-dynamic analysis of large frictional deformation was presented based on the Taylor-Galerkin method. An approach was proposed in modeling the thermal contact friction considering the perfect/imperfect thermal contact and dissipation phenomenon. The thermo-mechanical contact constraints were enforced by an optimized version of augmented-Lagrange technique based on the thermal contact resistance (TCR) approach for enforcing the heat flux continuity at the contact surface. It was shown that the convection term is dominant in the thermo-dynamic simulation and cannot be neglected from the heat transfer analysis due to stability issues in the classical time dependent algorithm. As a result, the Taylor-Galerkin approach was utilized for the time domain discretization of convection dominant problems. Finally, the capability of proposed computational algorithm was illustrated in the thermo-dynamic analysis of large frictional deformations. It was shown that the proposed model is capable of modeling the thermo-dynamic analysis of heat generation due to frictional dissipation, large frictional deformation, and contact-impact problems.

REFERENCES

1. Barber JR. The influence of thermal expansion on friction and wear process, *Wear*, **10**(1967) 155-9.
2. Carpenter NJ, Taylor RL, Katona MG. Lagrange constraints for transient finite-element surface-contact, *International Journal for Numerical Methods in Engineering*, **32**(1991) 103-28.
3. Cooper MG, Mikic BB, Yovanovich MM. Thermal contact conductance, *International Journal of Heat and Mass Transfer*, **12**(1969) 279-300.
4. Lorenzis L. de, Temizer I, Wriggers P, Zavarise G. A large deformation frictional contact formulation using NURBS-based isogeometric analysis, *International Journal for Numerical Methods in Engineering*, **87**(2011) 1278-300.
5. Saracibar CA de. Numerical analysis of coupled thermo-mechanical frictional contact problems – Computational model and applications, *Archives of Computational Methods in Engineering*, **5**(1998) 243-301.
6. Donea J. A Taylor-Galerkin method for convective transport problems, *International Journal for Numerical Methods in Engineering*, **20**(1984) 101-19.
7. Feng ZQ, Peyraut F, Labed N. Solution of large deformation contact problems with friction between Blatz-Ko hyperelastic bodies, *International Journal of Engineering Science*, **41**(2003) 2213-25.
8. Halikal G, Hjelmstad KD. A finite element formulation of non-smooth contact based on oriented volumes for quadrilateral and hexahedral elements, *Computer Methods in Applied Mechanics and Engineering*, **196**(2007) 4690-711.
9. Hlaváček I, Nedoma J. On a solution of a generalized semi-coercive contact problem in thermo-elasticity, *Mathematics and Computers in Simulation*, **60**(2002) 1–17.
10. Hlaváček I, Nedoma J. Reliable solution of an unilateral contact problem with friction

and uncertain data in thermo-elasticity, *Mathematics and Computers in Simulation*, **67**(2005) 559-80.

11. Hueber S, Wohlmuth B. Thermo-mechanical contact problems on non-matching meshes, *Computer Methods in Applied Mechanics and Engineering*, **198**(2009) 1338-50.
12. Khoei AR, Biabanaki SOR, Parvaneh SM. 3D dynamic modeling of powder forming processes via a simple and efficient node-to-surface contact algorithm, *Applied Mathematical Modelling*, (2012) doi.org/10.1016/ j.apm.2012.03.010.
13. Khoei AR, Keshavarz S, Khaloo AR. Modeling of large deformation frictional contact in powder compaction processes, *Applied Mathematical Modelling*, **32**(2008) 775-801.
14. Khoei AR, Mousavi SMT. Modeling of large deformation–large sliding contact via the penalty X-FEM technique, *Computational Materials Science*, **48**(2010) 471-80.
15. Laursen TA, Oancea VG. On the constitutive modeling and finite element computation of rate dependent frictional sliding in large deformations, *Computer Methods in Applied Mechanics and Engineering*, **143**(1997) 197-227.
16. Laursen TA, Simo JC. A continuum–based finite element formulation for the implicit solution of multibody, large deformation frictional contact problems, *International Journal for Numerical Methods in Engineering*, **36**(1993) 3451-85.
17. Morton KW. Numerical Solution of Convection-Diffusion Problems, Chapman and Hall, 1996.
18. Oancea VG, Laursen TA. A finite element formulation of thermo-mechanical rate-dependent frictional sliding, *International Journal for Numerical Methods in Engineering*, **40**(1997) 4275-311.
19. Oliver J, Hartmann S, Cante JC, Weyler R, Hernandez JA. A contact domain method for large deformation frictional contact problems, Part 1: Theoretical basis, *Computer Methods in Applied Mechanics and Engineering*, **198**(2009) 2591-606.
20. Padmanabhan V, Laursen TA. A framework for development of surface smoothing procedures in large deformation frictional contact analysis, *Finite Elements in Analysis and Design*, **37**(2001) 173-98.
21. Pantuso D, Bathe KJ, Bouzinov PA. A finite element procedure for the analysis of thermo-mechanical solids in contact, *Computers and Structures*, **75**(2000) 551-73.
22. Peric D, Owen DRJ. Computational model for 3D contact problems with friction based on the penalty method, *International Journal for Numerical Methods in Engineering*, **35**(1992) 1289-309.
23. Pietrzak G, Curnier A. Large deformation frictional contact mechanics: Continuum formulations and augmented-Lagrangian treatment, *Computer Methods in Applied Mechanics and Engineering*, **177**(1999) 351-81.
24. Rieger A, Wriggers P. Adaptive methods for thermo-mechanical contact problems, *International Journal for Numerical Methods in Engineering*, **59**(2004) 871-94.
25. Roig B. One-step Taylor-Galerkin methods for convection-diffusion problems, *Journal of Computational and Applied Mathematics*, **204**(2007) 95-101.
26. Simo JC, Laursen TA. An augmented Lagrangian treatment of contact problems involving friction, *Computers and Structures*, **42**(1992) 97-116.
27. Xing HL, Makinouchi A. Three dimensional finite element modeling of thermo-

mechanical frictional contact between finite deformation bodies using R-minimum strategy, *Computer Methods in Applied Mechanics and Engineering*, **191**(2002) 4193-214.

28. Yang B, Laursen TA, Meng X. Two dimensional mortar contact methods for large deformation frictional sliding, *International Journal for Numerical Methods in Engineering*, **62**(2005) 1183-225.
29. Yi YB. Finite element analysis of thermo-elastodynamic instability involving frictional heating, *Journal of Tribology*, **128**(2006) 718-24.